Absence of the threshold anomaly in the elastic scattering of the weakly bound projectile ^{7}Li on ^{27}Al

J. M. Figueira,* D. Abriola, J. O. Fernández Niello, A. Arazi, O. A. Capurro, E. de Barbará, G. V. Martí, D. Martínez Heimann, A. J. Pacheco, and J. E. Testoni

Laboratorio TANDAR, Comisión Nacional de Energía Atómica, Avenida General Paz 1499, 1650 San Martín, Buenos Aires, Argentina

I. Padrón,† P. R. S. Gomes, and J. Lubian

Instituto de Física, Universidade Federal Fluminense, Avenida Litoranea s/n, Gragoatá, Niterói, R. J., 24210-340, Brazil

(Received 19 December 2005; published 5 May 2006)

To study the conditions leading to the appearance of the threshold anomaly in systems involving weakly bound projectiles we measured elastic scattering cross sections for the ^{7}Li + ^{27}Al system at ten different bombarding energies. The results were exhaustively analyzed using different optical model potentials. The similar behavior observed in all these analyses allows us to conclude that no threshold anomaly is found for the present system.

DOI: 10.1103/PhysRevC.73.054603 PACS number(s): 25.70.Bc, 24.10.Ht, 25.70.Mn

I. INTRODUCTION

One of the most important features of the elastic scattering between heavy ions at energies close to the Coulomb barrier is the peculiar behavior of the optical potential, known as the threshold anomaly (TA) [1]. In brief, at higher energies the real and imaginary parts of the optical potential are energy independent; however, as the energy is lowered toward the Coulomb barrier, the imaginary part of the optical potential sharply decreases while, correspondingly, the real part presents a localized peak. This TA may be ascribed mainly to the coupling of the elastic scattering to other reaction channels that produces an attractive polarization potential ΔV, leading to the real potential $V_{\rm eff} = V_0 + \Delta V$, where V_0 is the real potential at higher energies. The behavior of the imaginary potential is associated with the closing of nonelastic peripheral channels at energies near and below the barrier. The behavior of the real potential is a manifestation of the physical concept of causality, which states that no reaction occurs before the matter wave reaches the scattering center. The mathematical relation involving causality and the TA is the dispersion relation [2], which connects the energy variation of the real potential to that of the imaginary potential through a principal value integral, as shown later in this paper, as Eq. (1). In addition, the strong channel effects connected with the TA also dictate the magnitude of enhancement of the sub-barrier fusion cross section, owing to the lowering of the Coulomb barrier that occurs when the attractive real part of the potential increases.

Although this effect is well established for the scattering of tightly bound nuclei, there are presently some speculative arguments and contradictory conclusions about the influence that the breakup of weakly bound nuclei might have on the TA [3–14]. For systems in which at least one of the participants is a weakly bound nucleus, it has been recently shown that the breakup cross section does not diminish so fast in the vicinity of the Coulomb barrier but, rather, that it can have values much larger than the fusion cross sections [15–21]. Therefore, for these nuclei, the rapid decrease of the fusion cross section does not imply the closing of all the reaction channels at sub-barrier energies. As a consequence of this large peripheral-reaction cross section at these energies, the imaginary part of the optical potential does not necessarily decrease and the TA may disappear. Moreover, it has been suggested [4,5] that the effect of coupling of the breakup channel to the continuum may produce a repulsive polarization potential that affects the overall dynamic polarization potential in such a way that the usual TA may vanish. This fact has been taken as a possible explanation of the absence of the usual TA for systems involving the weakly bound nuclei ^{6}Li or ^{7}Li such as ^{6,7}Li + ^{28}Si [9,10]. However, the available data for these projectiles are insufficient to predict under which conditions (e.g., a dependence on the target mass) the TA may be expected. For instance, the ^{7}Li + ^{208}Pb system shows a TA [4] whereas the ^{7}Li + ^{138}Ba system [5], recently re-analyzed using the São Paulo potential [22], does not. In the case of ^{6}Li the TA does not appear with either ^{208}Pb or ^{138}Ba targets.

For another weakly bound projectile, ^{9}Be, on the light target ^{27}Al, no evidence of a TA has been found [12]. Additionally, for the ^{9}Be + ^{64}Zn system, the observation of the TA depends on whether or not one considers a surface imaginary potential in addition to a volumetric imaginary potential [6]. In the study of the scattering of ^{9}Be on heavy targets, the usual threshold anomaly was found to be present for ^{208}Pb [11], whereas for the ^{209}Bi target [14] a very unusual behavior of the imaginary potential was observed, with an increase of its value as the energy decreases.

Part of the uncertainty in establishing whether the TA does in fact exist for a given system stems from the various approaches used to describe the elastic scattering data. Among the different descriptions one finds the use of double-folding potentials [4,9–11], Woods-Saxon potentials [5,6,8,12], and the parameter-free, nonlocal, double-folding São Paulo potential [12,13].

The purpose of the present work is to contribute to elucidating the conditions leading to the appearance of the TA in systems involving weakly bound projectiles. To this aim we have measured the elastic scattering in the ^{7}Li + ^{27}Al

*Electronic address: figueira@tandar.cnea.gov.ar
†Permanent address: CEADEN, PO Box 6122, Havana, Cuba.

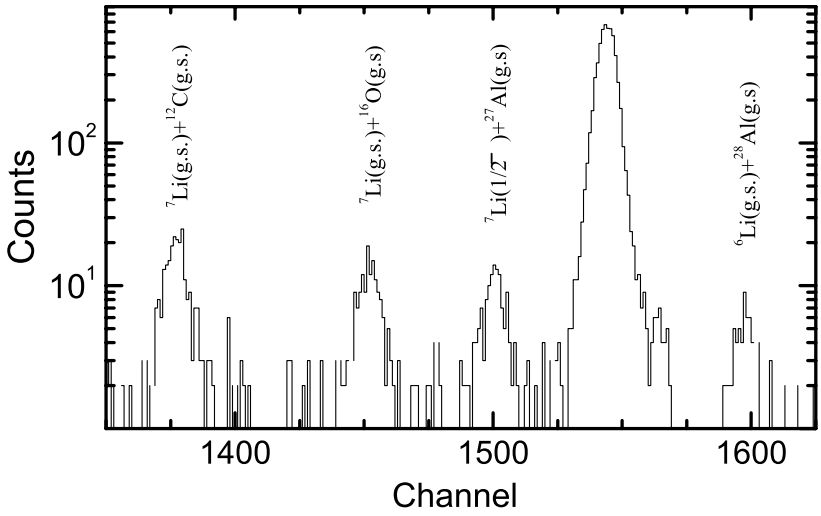

FIG. 1. Energy spectrum of the reaction products for ^{7}Li + ^{27}Al, measured at $E_{\rm Lab} = 18$ MeV and $\theta_{\rm c.m.} = 42.3^\circ$ around the elastic peak. Different exit channels are indicated in the figure.

system and we have analyzed the data using different approaches to check the consistency of the results. In the following section, the measurements are described; in Sec. III the data are analyzed with phenomenological and folding model potentials to verify whether the outcomes from all of them are similar. For this purpose different codes were also used (PTOLEMY [23] and ECIS [24]). Finally, in Sec. IV the results are discussed and our conclusions are given.

II. EXPERIMENTAL SETUP

Lithium-7 beams at bombarding energies of 6, 7, 8, 9, 10, 11, 12, 14, 16, and 18 MeV were delivered by the 20 UD tandem accelerator of the TANDAR Laboratory in Buenos Aires. Typical beam currents were below 50 nA. The nominal Coulomb barrier for the present reaction is around 8 MeV in the laboratory system. The Q value for the α-particle breakup of the projectile is -2.47 MeV.

A set of eight silicon surface-barrier detectors placed in a 30-in.-diameter scattering chamber was used to measure the elastic scattering cross sections at different angles. These angular distributions were taken in steps of 2°–5° depending on the energy and angular range. The angular resolution of each detector was less than 0.5° and their energy resolution ranged from 0.5 to 1%. The target was a 70 μg/cm^2 thick ^{27}Al foil. Although no direct charge identification was performed in this experiment, transfer and inelastic scattering channels can be easily separated from the elastic peak since they contribute to different position in the energy spectra, as is illustrated in Fig. 1. This figure, taken at $E_{\rm Lab} = 18$ MeV and $\theta_{\rm c.m.} = 42.3^\circ$, shows the position of the peaks corresponding to target contaminations (elastic scattering on ^{12}C and ^{16}O), as well as the one-neutron transfer and the inelastic scattering ^{27}Al(^{7}Li, ^{7}Li*(1/2$^-$, 0.477 MeV)).

Absolute values of the cross section were deduced by using an electron suppressed Faraday cup and a monitor detector at 15°. The estimated overall uncertainty of the results ranges from 5 to 15%. A summary of all the experimental results is displayed in Fig. 2, which shows the angular distributions of the elastic scattering cross sections normalized to the Rutherford cross section.

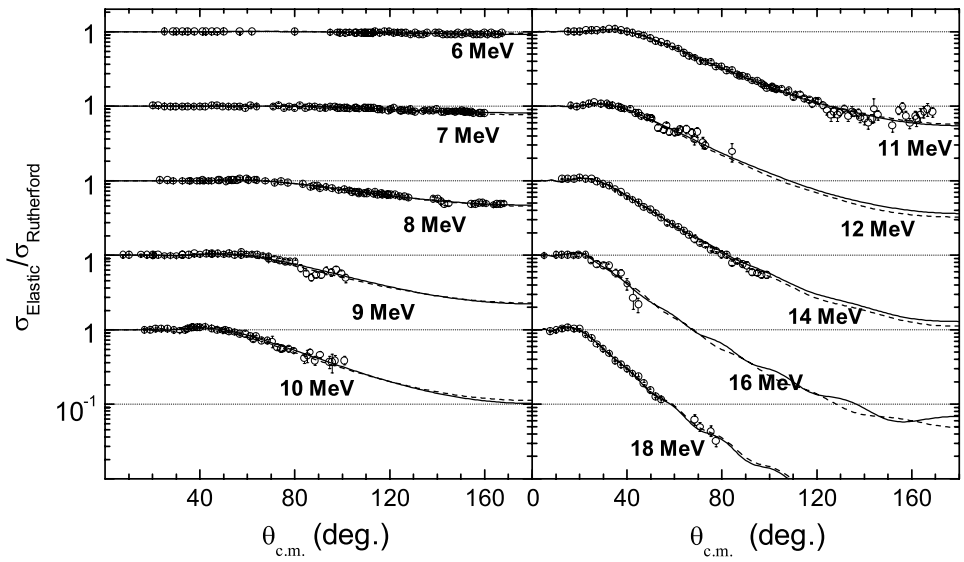

FIG. 2. Elastic scattering cross sections normalized to the Rutherford cross sections for the ^{7}Li + ^{27}Al system and optical model calculations. Full lines correspond to an energy-dependent fit whereas the dashed lines correspond to an energy-independent one. (For $E_{\rm Lab} = 6$, 8, and 9 MeV the two fits are almost indistinguishable.)

TABLE I. Parameters of the E I potential. The projectile energy and the potential depth are in MeV, the reduced radii and diffusenesses are in fm, and the volume integrals per nucleon pair are in MeV fm^3.

$E_{\text{c.m.}}$	V	r_0	a	WS	r_{si0}	a_{si}	W	r_{i0}	a_i	$[G(E)]_V$	$[G(E)]_{WT}$	χ^2/point
4.8	9.86	1.12	0.904	2.21	1.35	0.646	1.31	1.09	0.372	1.81	2.39	2.82
5.6												1.36
6.4												1.21
7.1												4.94
7.9												1.70
8.7												5.85
9.5												1.74
11.1												5.05
12.7												2.47
14.3												8.88

III. RESULTS AND OPTICAL MODEL ANALYSES

To analyze the elastic scattering cross sections we used (a) phenomenological potentials, (b) folding model potentials, in particular the so-called São Paulo potential, and (c) hybrid potentials, consisting of the São Paulo potential for the real part and a phenomenological potential for the imaginary part. For the phenomenological potentials we considered Woods-Saxon shapes in three different scenarios: (a.1) E I, an energy-independent potential, (a.2) EDFG, an energy-dependent potential with fixed geometric parameters (reduced radius and diffuseness), and (a.3) EDVG, an energy-dependent potential with variable geometric parameters.

In all cases, the essential features of the phenomenological potential were a real part with a shallow Woods-Saxon shape, with depth V, reduced radius r_0, and diffuseness a and an imaginary part composed of two terms, a volume term (also with a Woods-Saxon shape), with parameters W, r_{i0}, and a_i, and a surface term, described by WS, r_{si0}, and a_{si}. The volume term takes into account the fusion channel, whereas the surface term, which is proportional to the derivative of a Woods-Saxon shape, accounts for the flux of the quasi-elastic channels [25,26].

An energy-independent (E I) Woods-Saxon potential that reproduces the data quite well has been obtained from a global simultaneous fit to the data at all energies. The corresponding parameters and the resulting χ^2/point of the fits are presented in Table I. The experimental angular distributions and the results of the fit using this energy-independent potential are shown in Fig. 2 (dashed lines).

To explore for a possible energy dependence, a new parameter search was performed in which the depths of the real and imaginary surface parts of the potential were allowed to change independently at each energy. First, we studied the case where the reduced radii and diffusenesses were kept constant [energy-dependent fixed geometry (EDFG) potential]. The results of the corresponding energy-dependent fits are illustrated by the full line in Fig. 2. The depth of the real term varies between 6.5 and 12.6 MeV, and for the imaginary surface term between 1.6 and 8.9 MeV. The values of the depths, reduced radii, and diffusenesses of this potential are also shown in Table II. As can be seen, they represent only a slight improvement to the adjustment of the data compared to the energy-independent results.

The last phenomenological case was constructed taking the EDFG potential as a reference and allowing the geometric parameters to slightly change around those values. In this way, an energy-dependent variable geometry (EDVG) potential was obtained. As seen in Table III, this procedure yielded a slight decrease in the χ^2/point values.

TABLE II. Parameters of the EDFG potential. The projectile energy and the potential depth are in MeV, the reduced radii and diffusenesses are in fm, and the volume integrals per nucleon pair are in MeV fm^3.

$E_{\text{c.m.}}$	V	r_0	a	WS	r_{si0}	a_{si}	W	r_{i0}	a_i	$[G(E)]_V$	$[G(E)]_{WT}$	χ^2/point
4.8	6.5	1.12	0.904	8.9	1.35	0.646	1.31	1.09	0.372	1.2	9.6	1.23
5.6	6.7			1.9						1.2	2.1	0.72
6.4	9.3			2.5						1.7	2.7	1.11
7.1	8.7			1.6						1.6	1.7	4.48
7.9	8.1			1.6						1.5	1.8	0.82
8.7	10.4			2.2						1.9	2.4	2.67
9.5	8.4			2.3						1.5	2.5	1.38
11.1	10.2			2.5						1.9	2.7	3.69
12.7	12.6			2.9						2.3	3.2	1.77
14.3	10.0			2.1						1.8	2.3	8.53

TABLE III. Parameters of the EDVG potential. The projectile energy and the potential depth are in MeV, the reduced radii and diffusenesses are in fm, and the volume integrals per nucleon pair are in MeV fm^3.

$E_{\rm c.m.}$	V	r_0	a	WS	r_{si0}	a_{si}	W	r_{i0}	a_i	$[G(E)]_V$	$[G(E)]_{WT}$	χ^2/point
4.8	16.0	1.20	0.710	17.9	1.45	0.519	0.0038	1.09	0.372	2.4	25.7	1.17
5.6	6.9	1.15	0.778	1.2	1.40	0.703	0.0023			1.0	2.0	0.71
6.4	10.8	1.15	0.835	2.3	1.40	0.593	0.18			1.9	2.9	1.02
7.1	5.1	1.15	1.044	1.6	1.40	0.533	0.0024			1.6	1.7	3.99
7.9	7.4	1.12	1.023	3.0	1.40	0.405	1.31			2.0	1.8	0.41
8.7	10.5	1.12	0.917	2.3	1.35	0.625	1.31			2.1	2.4	2.58
9.5	13.7	1.12	0.913	4.7	1.35	0.450	1.31			2.7	2.3	0.93
11.1	9.3	1.12	0.908	2.9	1.30	0.721	1.31			1.8	3.0	1.97
12.7	13.6	1.12	0.733	2.5	1.30	0.800	1.31			1.5	3.2	1.22
14.3	10.5	1.09	0.899	2.0	1.35	0.699	1.655			1.7	2.7	7.68

To compare different potentials, it is useful to calculate the sensitivity radius R_S [25,26], which corresponds to the radius at which potentials with comparable good fits take approximately the same value. For the real part, this sensitivity radius was determined at each energy by selecting a set of slightly modified diffuseness parameters a (taken in steps of 0.05 fm around the best value) and adjusting the radius parameter and the potential depth to fit the data. In this way, different families of optical model potentials with roughly the same χ^2/point value were obtained. The same procedure was done to obtain the sensitivity radii for the imaginary part. Figure 3 shows the crossing points of the real and imaginary potentials for different families of parameters for the EDFG case corresponding to the fits of the $E_{\rm c.m.} = 7.9$ MeV data.

In what follows, we analyze whether the obtained energy-dependent potentials satisfy the dispersion relation, which connects the real and imaginary parts through the expression (except for a constant offset)

$$V(r, E) = P\frac{1}{\pi}\int \frac{W(r, E')}{E' - E}dE', \qquad (1)$$

where P denotes the principal value. For this purpose it is customary to evaluate Eq. (1) at the sensitivity radius. However, as illustrated in Fig. 4, the sensitivity radii at different energies are not strictly constant but they fluctuate around a given value. This problem might be overcome by applying the alternative method to evaluate the dispersion relation used by Brandan *et al.* [27]. It can be shown [28,29] that the dispersion relation still holds for the volume integrals per nucleon pair weighted by a Gaussian function $g(r)$ centered at an average value $\overline{R}_S$ and with a width σ. The two volume integrals are $[G(E)]_V$ and $[G(E)]_{WT}$, with $WT(r) = W(r) + WS(r)$. The

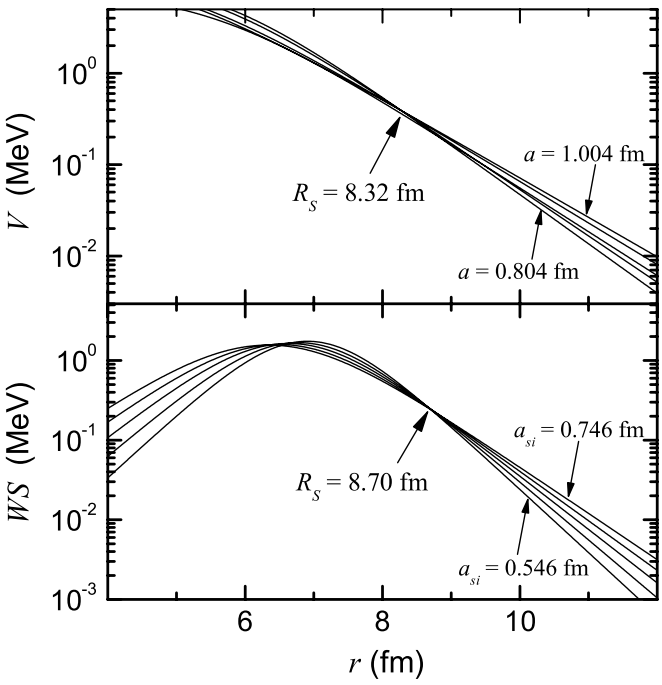

FIG. 3. Sensitivity radius based on the crossing of the real (upper) and imaginary (lower) parts of the EDFG potential at $E_{\rm Lab} = 10$ MeV. The real and imaginary diffusenesses, a and a_{si}, were varied in steps of 0.05 fm between 0.804 and 1.004 fm, and between 0.546 and 0.746 fm, respectively.

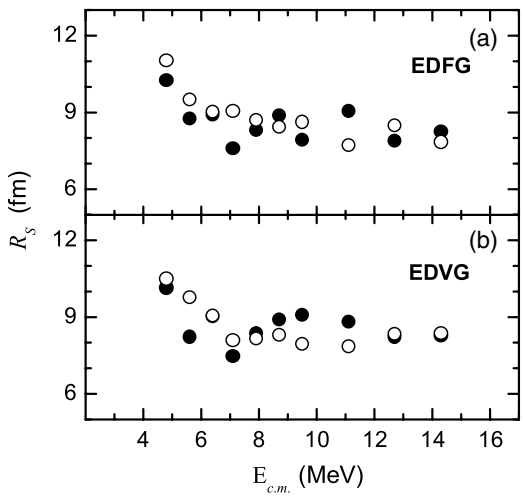

FIG. 4. Radii of sensitivity, R_S, as a function of the c.m. energy for (a) the EDFG case and (b) the EDVG case. Full circles correspond to the radii of sensitivity for the real part of the optical potential whereas open circles correspond to the imaginary part.

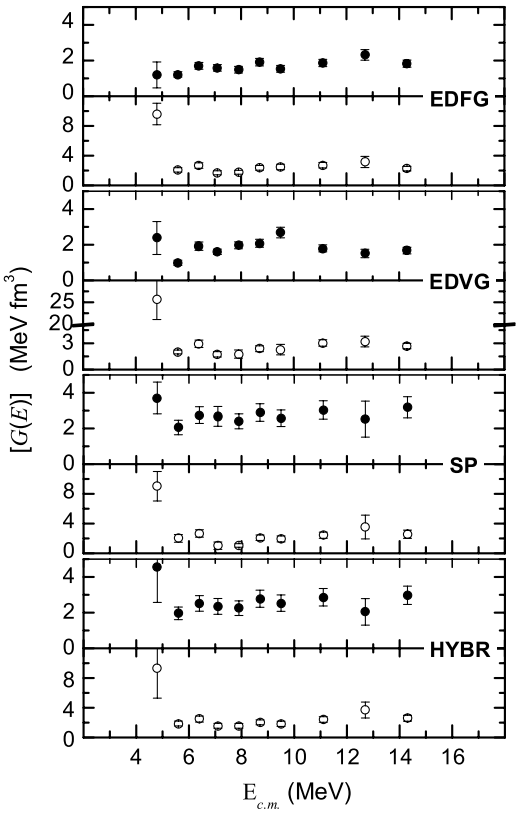

FIG. 5. Volume integrals $[G(E)]$ around the sensitivity radius calculated for the real (full circles) and imaginary (open circles) parts of the different potentials analyzed in this work.

volume integral for the real potential is defined by

$$[G(E)]_V = \frac{1}{A_p \times A_t} \int V(r, E) g(r) 4\pi r^2 dr, \qquad (2)$$

where $A_p = 7$ and $A_t = 27$ are the projectile and target mass numbers respectively. There is a similar equation for $[G(E)]_{WT}$. Therefore, a dispersion relation in the form of

$$[G(E)]_V = P\frac{1}{\pi} \int \frac{[G(E')]_{WT}}{E' - E} dE', \qquad (3)$$

which is analogous to Eq. (1), must hold.

To calculate the parameters of the Gaussian distribution, $g(r)$, we have assumed a normal distribution for the sensitivity radius (see Ref. [27]). We calculated the average radius and the standard deviation by taking $N = 18$ points. The radii corresponding to the lowest energy ($E_{\text{c.m.}} = 4.8$ MeV) were not taken into account since they deviate considerably from the average value. The average radius and standard deviations obtained for the EDFG and for the EDVG potentials are $\overline{R}_S = 8.50 \pm 0.13$ fm, $\sigma = 0.54^{+0.10}_{-0.09}$ fm, and $\overline{R}_S = 8.46 \pm 0.13$ fm, $\sigma = 0.55^{+0.10}_{-0.09}$ fm, respectively. The uncertainties in these quantities have been estimated by means of a Student's t and a χ^2 distributions of $N - 1$ degrees of freedom, respectively. The intervals correspond to a confidence level of 70%.

The uncertainties in the real and imaginary potential depths were obtained by varying the parameters up to the point in which the total χ^2 value of the fit increases in one unit, which also corresponds to a confidence level of 68.3%. The results of these integrals are shown in Fig. 5. The error bars stem from the root sum square of the contributing uncertainties in the potential depths, in the average radius, and in the standard deviation.

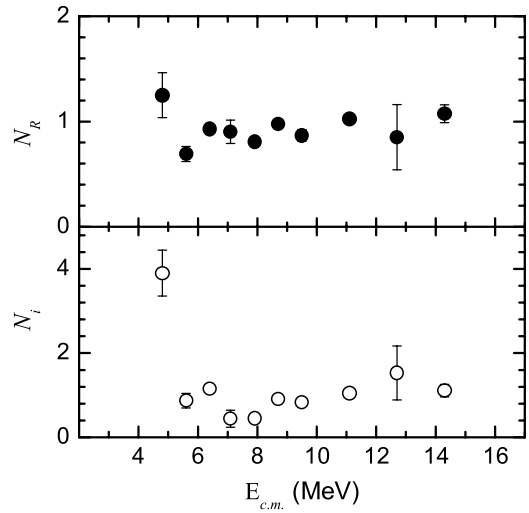

FIG. 6. Normalization factors N_R and N_i of the São Paulo potential that best reproduce the data.

The volume integrals of the real and imaginary parts of the energy-dependent potentials do not show the usual threshold anomaly. In other words, the imaginary potential is almost constant as a function of the energy except for the lowest measured energy ($E_{\text{c.m.}} = 4.8$ MeV), which lies well above the rest. This point has a large error bar because the elastic scattering cross section at this energy corresponds to almost

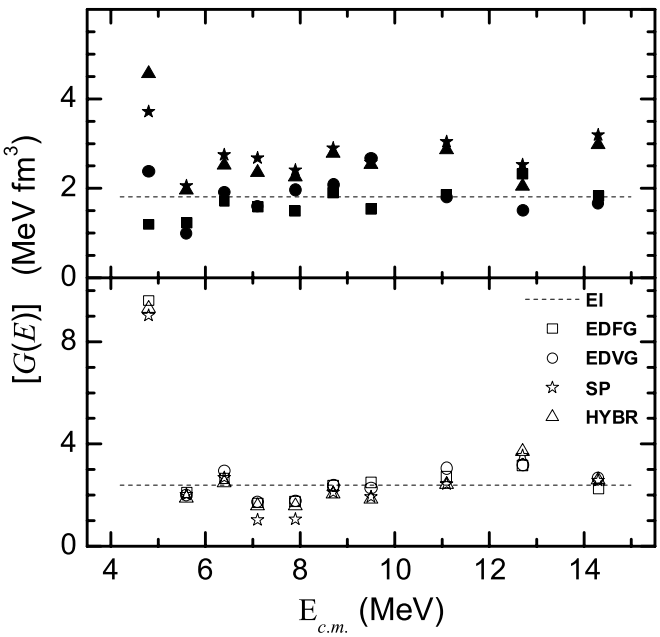

FIG. 7. Volume integrals $[G(E)]$ as in Fig. 5, for the real (full symbols) and imaginary (open symbols) parts of the different potentials. Error bars are omitted for clarity and the values for the E I potential are included for comparison.

TABLE IV. Normalization factors for the SP potential. The projectile energy is in MeV and the volume integrals per nucleon pair are in MeV fm^3.

$E_{\text{c.m.}}$	N_R	N_i	$[G(E)]_V$	$[G(E)]_{WT}$	χ^2/point
4.8	1.25	3.90	3.7	9.0	1.29
5.6	0.69	0.87	2.1	2.0	0.72
6.4	0.93	1.15	2.7	2.7	1.12
7.1	0.90	0.44	2.7	1.0	4.30
7.9	0.81	0.46	2.4	1.1	0.81
8.7	0.98	0.91	2.9	2.1	3.65
9.5	0.87	0.83	2.6	1.9	1.29
11.1	1.02	1.05	3.0	2.4	2.60
12.7	0.85	1.53	2.5	3.5	1.96
14.3	1.07	1.11	3.2	2.6	23.9

pure Rutherford scattering. The same constant behavior is true for the real part of the potential, except for the lowest measured energy as in the imaginary case.

Both Woods-Saxon potentials have very shallow depths, typically around a few MeV. We have also tried deeper potentials obtained from first-principle calculations such as the São Paulo potential, which is a global parameter-free optical potential [30–34] able to describe a large variety of systems in a very wide energy range. In the construction of this potential, the real and imaginary parts of the optical potential (which were assumed to have the same radial shape) were derived in the framework of an extensive systematization of nuclear densities and the energy dependence of the bare potential was accounted for by a model based on the nonlocal nature of the interaction. The bare interaction V_N takes into account the Pauli nonlocality involving the exchange of nucleons between projectile and target, and it is connected with the folding potential V_F through

$$V_N(R, E) \approx V_F(R) \exp(-4v^2/c^2), \tag{4}$$

where c is the speed of light in vacuum and v is the local relative velocity between the two nuclei,

$$v^2(R, E) = (2/\mu)[E - V_C(R) - V_N(R, E)], \tag{5}$$

with μ the reduced mass and V_C the Coulomb interaction.

The folding potential, obtained by using the matter distributions of the nuclei, which take into account the finite size of the nucleon, with a zero-range approach for the nucleon-nucleon interaction $v(r)$, is

$$V_F(R) = \int \rho_1(r_1)\rho_2(r_2)v(R - r_1 - r_2)dr_1dr_2. \tag{6}$$

For V_C a double sharp-cutoff Coulomb potential was used. To obtain a global parameter-free description of the nuclear interaction, a systematization of nuclear densities was developed. This system was based on an extensive study involving charge distributions extracted from electron scattering data and theoretical densities calculated through the Dirac-Hartree-Bogoliubov model and adopts the two-parameter Fermi (2pF) distribution to describe the nuclear densities. Within the derived systematization, the radii of the 2pF distributions of a nucleus with A nucleons are well described by

$$R_0 = (1.31A^{1/3} - 0.84)\,\text{fm}, \tag{7}$$

and the matter densities have an average diffuseness of $a = 0.56$ fm. The imaginary part of the interaction is assumed to have the same shape of the real part [Eq. (4)], with one single adjustable parameter N_i related to its strength, such as

$$W(R, E) = N_i V_N(R, E). \tag{8}$$

For more than 30 systems, all the elastic scattering angular distributions, over wide energy ranges, were simultaneously well fitted with only one free parameter, the average value of N_i, which was derived to be $N_i = 0.78$.

When this potential is calculated for the ^{7}Li + ^{27}Al system it has a large depth in both the real and the imaginary parts (around 293 MeV). The resulting fits of the normalization factors for the real and imaginary parts (N_R and N_i, respectively) are shown in Fig. 6 and in Table IV. It can be seen that their energy dependence follows the same constant trend as the previous calculations displayed in Fig. 5. These data could be directly compared with the other potentials by calculating the volume integrals for these deep potentials. The results are shown in Fig. 5.

Finally, we also tried an approach that combines both potentials, the São Paulo and the Woods-Saxon potentials.

TABLE V. Parameters of the HYBR potential. The projectile energy and the potential depths *WS* and *W* are in MeV, the reduced radii and diffusenesses are in fm, and the volume integrals per nucleon pair are in MeV fm^3.

$E_{\text{c.m.}}$	N_R	WS	r_{si0}	a_{si}	W	r_{i0}	a_i	$[G(E)]_V$	$[G(E)]_{WT}$	χ^2/point
4.8	2.19	8.14	1.30	0.699	50	0.998	0.688	4.6	9.3	1.19
5.6	0.94	0.32						2.0	1.9	0.72
6.4	1.21	0.96						2.5	2.5	1.13
7.1	1.13	0.00						2.4	1.6	4.46
7.9	1.08	0.00						2.3	1.6	1.02
8.7	1.33	0.49						2.8	2.0	3.68
9.5	1.22	0.29						2.5	1.8	1.32
11.1	1.37	0.89						2.9	2.4	2.45
12.7	0.98	2.24						2.0	3.7	1.85
14.3	1.43	1.07						3.0	2.6	22.9

TABLE VI. Global χ^2/point and summary of the parameters for the different optical potentials used in the data analyses. The values for the anomalous point at the lowest energy have been excluded. The potentials depth are in MeV and the reduced radii and diffusenesses are in fm.

Potential	V	r_0	a	WS	r_{si0}	a_{si}	W	r_{i0}	a_i	Global χ^2/point
E I	9.86	1.12	0.904	2.21	1.35	0.646	1.31	1.09	0.372	3.89
EDFG	6.7–12.6	1.12	0.904	1.6–2.9	1.35	0.646	1.31	1.09	0.372	2.34
EDVG	5.1–13.7	1.09–1.15	0.73–1.04	1.2–4.7	1.30–1.40	0.45–0.80	0.02–1.65	1.09	0.372	1.96
SP	—	—	—	—	—	—	—	—	—	3.26
HYBR	—	—	—	0.00–2.24	1.3	0.699	50	0.998	0.688	3.23

This hybrid potential was formed by taking a deep real part (from the São Paulo potential) and a rather shallow imaginary potential. The latter was adjusted to obtain the best optical model parameters, which are shown in Table V (labeled as the HYBR case). The results from this analysis, which are also presented in Fig. 5, show a rather smooth energy dependence of the real and imaginary parts of the optical potential, except for the lowest measured distribution at the sub-barrier energy of $E_{\text{c.m.}} = 4.8$ MeV.

The results of the volume integrals shown in Fig. 5 for all the potentials used in this work are consistent and indicate that no threshold anomaly is present for this system. Table VI summarizes the results for all the potentials and includes the global χ^2/point for the fit at all energies corresponding to each potential. The values of the imaginary potential at $E_{\text{c.m.}} = 4.8$ MeV are consistently larger than the values at higher energies for all the examined potentials. Although this systematic behavior cannot be explained at present, it does not affect the main conclusions that follow.

To further stress the absence of the threshold anomaly in this system, the volume integrals for the five potentials studied are presented superimposed in Fig. 7. It is seen in this figure that not only is the shape of the energy dependence the same for all potentials—being, constant as a function of energy—but even the absolute values of the volume integrals are about the same for all potentials. This fact is of course what one expects, but to actually find such an agreement among the results of very different potentials is nonetheless remarkable.

IV. CONCLUSIONS

The absence of a threshold anomaly in the elastic scattering of some reaction systems that involve weakly bound nuclei is usually interpreted as evidence of the role played by the breakup channel at sub-barrier energies. However, the conditions under which the TA does indeed appear are not clear and may depend in particular on the type of approach used in the analysis. To contribute to clarifying these matters we measured elastic scattering cross sections for the $^7\text{Li} + ^{27}\text{Al}$ system at energies around the Coulomb barrier and analyzed the data using different approaches. The present analysis suggests that no threshold anomaly is found for this system. This result seems to be quite independent of the different families of potential used. From the experimental point of view, new experiments to measure the $^6\text{Li} + ^{27}\text{Al}$ system as well as a direct measurement of the breakup cross section are in progress.

ACKNOWLEDGMENTS

Some of us (I.P., P.R.S.G., and J.L.) acknowledge the financial support of the CNPq (Brazil) and CLAF (I.P.). J.O.F.N., A.J.P., and J.E.T. are also members of the Consejo Nacional de Investigaciones Científicas y Técnicas, Argentina.

[1] G. R. Satchler, Phys. Rep. **199**, 147 (1991).
[2] M. A. Nagarajan, C. C. Mahaux, and G. R. Satchler, Phys. Rev. Lett. **54**, 1136 (1985).
[3] L. F. Canto, P. R. S. Gomes, R. Donangelo, and M. S. Hussein, Phys. Rep. **424**, 1 (2006).
[4] N. Keeley *et al.*, Nucl. Phys. **A571**, 326 (1994).
[5] A. M. M. Maciel *et al.*, Phys. Rev. C **59**, 2103 (1999).
[6] S. B. Moraes *et al.*, Phys. Rev. C **61**, 064608 (2000).
[7] K. Rusek and K. W. Kemper, Phys. Rev. C **61**, 034608 (2000).
[8] J. Lubian *et al.*, Phys. Rev. C **64**, 027601 (2001).
[9] A. Pakou *et al.*, Phys. Lett. **B556**, 21 (2003).
[10] A. Pakou *et al.*, Phys. Rev. C **69**, 054602 (2004).
[11] R. J. Woolliscroft *et al.*, Phys. Rev. C **69**, 044612 (2004).
[12] P. R. S. Gomes *et al.*, Phys. Rev. C **70**, 054605 (2004).
[13] P. R. S. Gomes *et al.*, Phys. Rev. C **71**, 034608 (2005).
[14] C. Signorini *et al.*, Phys. Rev. C **61**, 061603(R) (2000).
[15] D. J. Hinde *et al.*, Phys. Rev. Lett. **89**, 272701 (2002).
[16] E. F. Aguilera *et al.*, Phys. Rev. C **63**, 061603(R) (2001).
[17] Y. W. Wu *et al.*, Phys. Rev. C **68**, 044605 (2003).
[18] P. R. S. Gomes *et al.*, Phys. Lett. **B601**, 20 (2004).
[19] G. V. Martí *et al.*, Phys. Rev. C **71**, 027602 (2005).
[20] P. R. S. Gomes *et al.*, Phys. Lett. **B634**, 356 (2006).
[21] R. J. Woolliscroft *et al.*, Phys. Rev. C **68**, 014611 (2003).
[22] P. R. S. Gomes *et al.*, J. Phys. G: Nucl. Part. Phys. **31**, S1669 (2005).
[23] M. H. MacFarlane *et al.*, Argonne National Laboratory Report **ANL-76-11**, 1983, Rev. 1 (unpublished).
[24] J. Raynal, Phys. Rev. C **23**, 2571 (1981).
[25] D. Abriola *et al.*, Phys. Rev. C **39**, 546 (1989).
[26] D. Abriola *et al.*, Phys. Rev. C **46**, 244 (1992).
[27] M. E. Brandan *et al.*, Phys. Rev. C **48**, 1147 (1993).

[28] C. Mahaux, H. Ngo, and G. R. Satchler, Nucl. Phys. **A449**, 354 (1986).
[29] C. Mahaux, H. Ngo, and G. R. Satchler, Nucl. Phys. **A456**, 134 (1986).
[30] L. C. Chamon *et al*., Phys. Rev. C **66**, 014610 (2002).
[31] M. A. G. Alvarez *et al*., Nucl. Phys. **A723**, 93 (2003).
[32] M. A. Candido Ribeiro, L. C. Chamon, D. Pereira, M. S. Hussein, and D. Galetti, Phys. Rev. Lett. **78**, 3270 (1997).
[33] L. C. Chamon, D. Pereira, M. S. Hussein, M. A. Candido Ribeiro, and D. Galetti, Phys. Rev. Lett. **79**, 5218 (1997).
[34] L. C. Chamon, D. Pereira, and M. S. Hussein, Phys. Rev. C **58**, 576 (1998).